

ARTICLE OPEN



Robust and tunable Weyl phases by coherent infrared phonons in ZrTe_5

Niraj Aryal¹✉, Xilian Jin^{1,2}, Qiang Li^{1,3}, Mengkun Liu³, A. M. Tselik¹ and Weiguo Yin¹✉

Ultrafast control of structural and electronic properties of various quantum materials has recently sparked great interest. In particular, photoinduced switching between distinct topological phases has been considered a promising route to realize quantum computers. Here we use first-principles and effective Hamiltonian methods to show that in ZrTe_5 , lattice distortions corresponding to all three types of zone-center infrared optical phonon modes can drive the system from a topological insulator to a Weyl semimetal. Thus achieved Weyl phases are robust, highly tunable, and one of the cleanest due to the proximity of the Weyl points to the Fermi level and a lack of other carriers. We also find that Berry curvature dipole moment, induced by the dynamical inversion symmetry breaking, gives rise to various nonlinear effects that oscillate with the amplitude of the phonon modes. These nonlinear effects present an ultrafast switch for controlling the Weyltronics-enabled quantum system.

npj Computational Materials (2022)8:113; <https://doi.org/10.1038/s41524-022-00800-z>

INTRODUCTION

Topological materials, such as Dirac and Weyl semimetals, and topological insulators, have attracted monumental research efforts thanks to their properties and potential for energy and quantum information applications^{1,2}. Despite profound challenges, quantum information has become a major thrust in this field due to the robustness of the topological states^{3,4}, highly desirable for high-temperature fault-tolerant multi-qubit computation and communication^{5–7}. The fast operation on the qubits requires a quantum material that can be easily driven from one topological phase to another by small controllable stimuli, in particular by the ultrafast laser pumping^{8–10}. It would be highly desirable to have a clean system that unambiguously displays signatures of the topological characters in different transport phenomena.

Zirconium pentatelluride (ZrTe_5) is a tunable topological material ideally suited for studying different topological phases due to its proximity to the phase boundary between the weak topological insulator (WTI) and the strong topological insulator (STI)^{11–14}. Owing to the small bandgap (~ 20 meV) and layered geometry, small external perturbations such as strain and temperature can drive this system from the STI to WTI regime with Dirac semimetal (DSM) as a critical point^{15,16}. By breaking time-reversal symmetry, magnetic fields of a few Tesla were predicted to change the system to Weyl and nodal line semimetal depending on the direction of the field¹⁷ and a chiral magnetic effect in electron transport was observed¹².

Recently, it was shown that the STI-DSM-WTI transition can be achieved in ZrTe_5 by photoexciting various combinations of the Raman phonon modes^{18–20}, which preserves the inversion symmetry. Since 4×4 Dirac Hamiltonian (massive or massless) can become 2×2 Weyl Hamiltonians separated in k -space if either time-reversal or inversion symmetry is broken, this suggests that it might be possible to achieve a Weyl semimetallic phase by breaking inversion symmetry^{21,22} with infrared (IR) phonon modes in ZrTe_5 ^{18,23}. Luo et al.²⁴ have demonstrated that nonlinear photocurrent and chiral charge pumping in ZrTe_5 could be

generated by using a circularly polarized high-intensity (with a fluence of $\sim 1 \text{ mJ cm}^{-2}$) 800 nm laser source that appeared to induce the lowest IR phonon mode. While bulk photocurrent generation in inversion asymmetric crystals has been known for quite some time^{25,26}, the above experimental observation manifests photocurrent generation in an inversion symmetric material. Its significance in light-controlled quantum topological switches makes it urgent for a thorough investigation of the IR phonon-induced topological phase transition and related transport signatures in ZrTe_5 . For example, it is not obvious if the photocurrent generation process and the topological phase transition to the Weyl semimetallic phase reported in ref. ²⁴ is specific to a particular IR phonon mode or a general behavior induced by all (or several different combinations) of the IR modes due to the breaking of the underlying crystal inversion symmetry. The later possibility will be particularly useful for photocurrent engineering and optimisation. Another key issue is the high cost of the high intensity (or fluence) laser sources used to drive dynamical inversion asymmetry in such ultrafast experiments. Hence it is important to figure out whether it is possible to generate photocurrent as well as drive the system to the topological phase transition by a smaller lattice distortion. Finally, it is intriguing to explore the role of the Fermi surface and the Weyl points (WPs) in the second order nonlinear phenomena such as photocurrent and nonlinear Hall effect.

In this article, we address these questions by performing a systematic computational and theoretical study of ZrTe_5 under adiabatic atomic displacement corresponding to the IR optical phonon modes. Time-dependent density functional theory calculations²⁷ showed how femtosecond laser pulses with circularly polarized light can turn the Dirac semimetal into the Weyl semimetal in Na_3Bi , a symmetry-protected three-dimensional Dirac semimetal^{28,29}, while linearly polarized pumping can induce a symmetry breaking field that destroys the Dirac point and opens a gap. The further justification for our approach comes from the ultrafast experiments which have demonstrated the

¹Condensed Matter Physics and Materials Science Division, Brookhaven National Laboratory, Upton, NY 11973, USA. ²State Key Laboratory of Superhard Materials, College of Physics, Jilin University, Changchun 130012, China. ³Department of Physics and Astronomy, Stony Brook University, Stony Brook, NY 11794, USA. ✉email: naryal@bnl.gov; wyin@bnl.gov

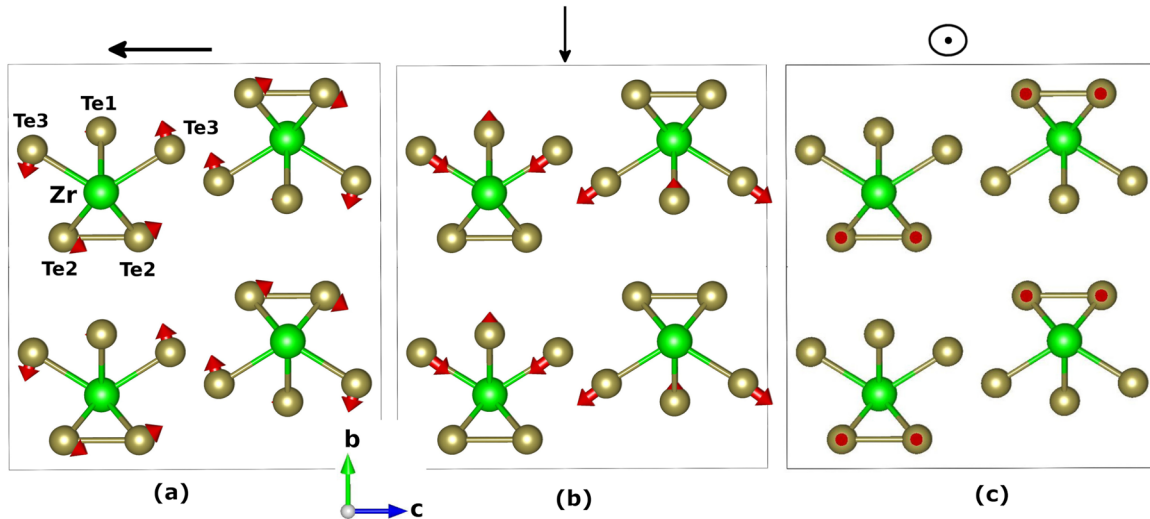


Fig. 1 Three different types of IR phonon modes of ZrTe_5 projected onto the b - c plane with the vectors showing the normal atomic displacement. **a** B_{1u} -4 **b** B_{2u} -20 and **c** B_{3u} -8 modes with frequencies of 0.58, 3.04, and 1.38 THz respectively. The atomic displacements in panel (c) are perpendicular to the b - c plane, hence the vectors are not seen in the figure. The black arrow at the top of each figure shows net polarization direction. For all the B_{1u} , B_{2u} and B_{3u} phonon modes, the net polarization direction is along c , b , and a -axis, respectively.

existence of a long-lived (100–200 ps) photoinduced transient electronic state in ZrTe_5 ^{20,24}, accompanied by a similarly long-lived shifting of the atomic positions¹⁹. This long thermalization time is consistent with the low electronic density of the states at the tip of the Dirac cone.

We have found that (i) atomic displacements corresponding to all possible types of Γ -centered IR phonon modes in ZrTe_5 introduce inversion asymmetry in only three possible ways; all these three types of IR modes dynamically drive the system from STI to the Weyl phase, (ii) these dynamical Weyl phases exist only when the magnitude of the normal atomic displacements (or equivalently lattice distortion) exceeds a certain threshold which magnitude depends on the details of the phonon modes; then such Weyl phases are robust over a large value of the lattice distortion and are highly tunable in the number and position, (iii) the magnitude of lattice distortion, which is determined by the fluence of the laser source used in the experiments, can be dramatically reduced if the system is in close vicinity to the Dirac semimetallic (DSM) phase, and (iv) while the phonon-driven inversion asymmetry naturally leads to the nonlinear responses induced by the non-zero Berry curvature, the occurrence of the WPs in the vicinity of the Fermi surface significantly changes their magnitude and direction. Such tunable nonlinear responses may find applications in various quantum switches³⁰. We believe that the proximity of the dynamical WPs to the Fermi level and lack of other trivial carriers make the phonon-driven ZrTe_5 an ideal platform for understanding and verification of many intriguing physical properties often attributed to the presence of the WPs.

RESULTS

Crystal structure and IR phonon modes

ZrTe_5 crystallizes in orthorhombic Cmcm space group (see Supplementary Note 1). The primitive unit cell contains 2 formula units and thus $N_{\text{atoms}} = 12$. The calculated phonon band structure was reported in ref. 18. The 36 phonon modes of ZrTe_5 at the Γ -point can be written into the following irreducible representations of the isomorphic point group D_{2h} ³¹:

$$\begin{aligned} \Gamma_{\text{acoustic}} &= B_{1u} + B_{2u} + B_{3u}, \\ \Gamma_{\text{optical}} &= 6A_g + 2A_u + 4B_{1g} + 5B_{1u} + 2B_{2g} \\ &\quad + 5B_{2u} + 6B_{3g} + 3B_{3u}, \end{aligned} \quad (1)$$

where g and u stand for Raman and IR modes respectively and A and B modes denote symmetry and anti-symmetry with respect to the twofold symmetry axes. The A_u modes are optically inactive. The phonons at the Γ -point can further be divided into groups of modes perpendicular and parallel to the chain direction, i.e., a -axis³¹:

$$\begin{aligned} \Gamma_{\parallel\text{chain}} &= 4B_{1g} + 2B_{2g} + 4B_{3u} + 2A_u, \\ \Gamma_{\perp\text{chain}} &= 6A_g + 6B_{1u} + 6B_{2u} + 6B_{3g}. \end{aligned} \quad (2)$$

In this study, we focus on the optically active IR modes which break global inversion symmetries. There are three types of IR modes: B_{1u} , B_{2u} , and B_{3u} . Each of these IR modes break one mirror symmetry in the reciprocal space in addition to the inversion symmetry. In Fig. 1, we present the vibration modes of the three different types of IR modes projected on the b - c plane (see Supplementary Fig. 3 for individual IR modes). From now on, these Γ -point IR modes are labeled depending on their symmetry and order in energy which are tabulated in Supplementary Table 2.

Topological phase transition

In this section, we present our DFT calculated electronic dispersions in the vicinity of the Γ -point as a function of $Q_{\mathbf{k}=\Gamma}^{(l)}$ (written as Q for convenience) which is the amplitude of oscillation (lattice distortion) of the l^{th} phonon mode with frequency $\omega^{(l)}$ at the Γ -point. Q is expressed in units of $\text{\AA} \text{amu}^{\frac{1}{2}}$ such that the energy cost of the lattice distortion corresponding to the l -th phonon mode is given by $E^{(l)} = \frac{1}{2}\omega^{(l)2}Q^{(l)2}$. We determine the critical value of Q (Q_c) required for the formation of the Weyl points (WPs) and track their evolution (creation/annihilation and position) as a function of Q for all three types of IR modes.

We find that all IR modes studied in this work drive the system from STI to the Weyl phase for $Q \sim 1$ except one IR mode which will be discussed more in the next section. Thus formed WPs are robust over a fairly large value of Q . The microscopic mechanism for the formation of the WPs is similar to all the IR modes; there is a transfer of charge from Te2 to Te3 atoms. Also only two pairs of WPs are formed which is the minimum number of WPs possible for the inversion symmetry broken system. The exact position of the WPs for different IR modes as a function of Q is tabulated in Supplementary Table 4. The location of the WPs is consistent with our findings from the model Hamiltonian which will be discussed in the next section. When the WPs finally gap out, the system goes

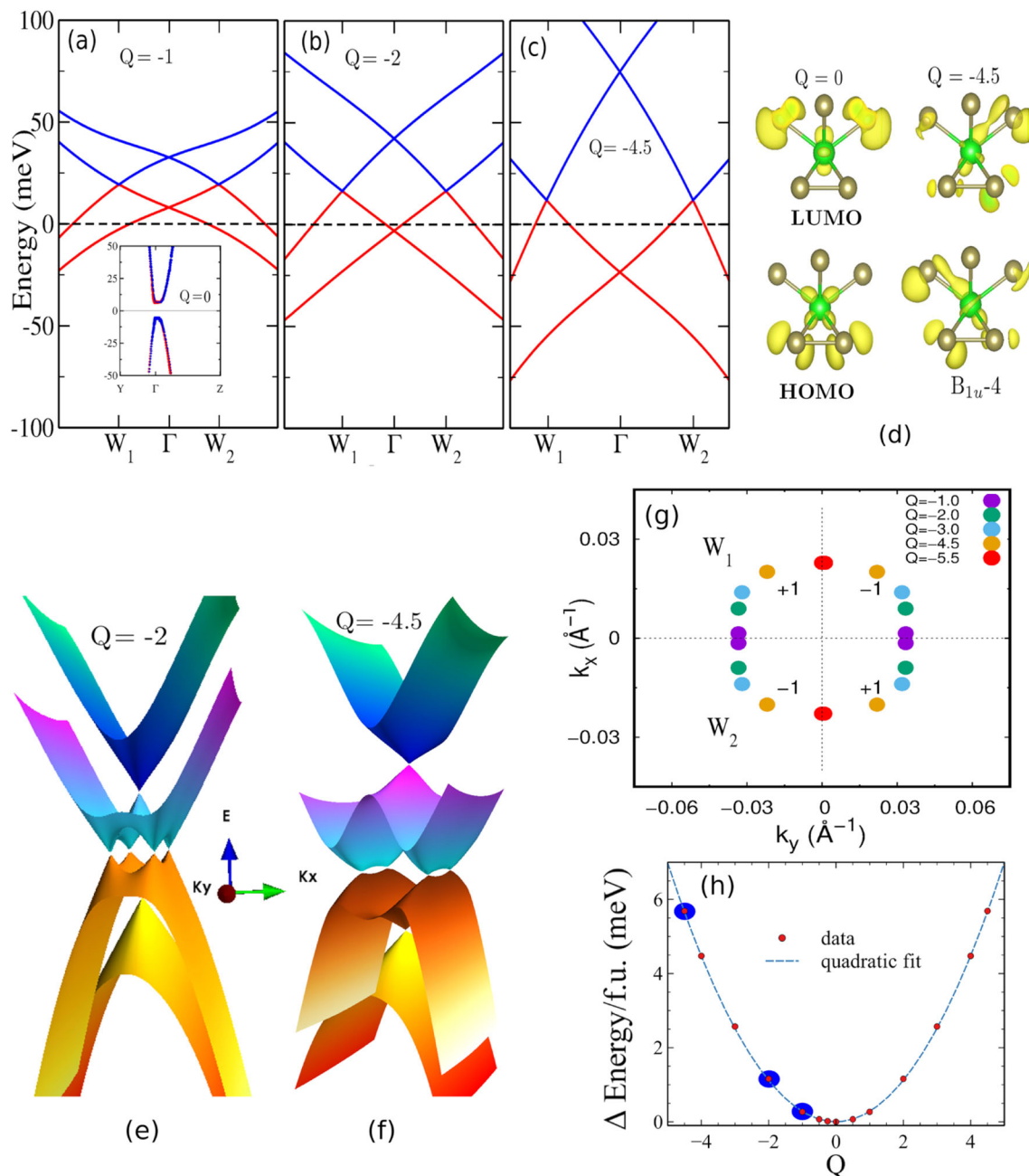


Fig. 2 B_{1u} phonon mode and Weyl bands. **a–c** Band structure along W_1 - Γ - W_2 direction for different Q values corresponding to the B_{1u-4} phonon mode. W_1 and W_2 are the sink and source of the Berry curvature separated along the k_y direction (panel **g**). The inset in **(a)** shows the ground state bands (i.e., $Q = 0$) in the vicinity of the Γ -point along with the Te3 (red dots) and Te2 (blue dots) band characters. **d** Charge density plot of the HOMO and LUMO states at the Γ point showing the transfer of charge from Te2 to Te3 atoms for nonzero Q . **e, f** 2D bands forming the WPs on the k_x - k_y (k_a - k_b) plane for different Q values. Note that the finite gaps seen in the Weyl bands are due to the finite k -point mesh in the calculation. The presence of Weyl points was confirmed by calculating the topological charges. **g** Evolution of the WPs as a function of Q . ± 1 indicates the chirality of the WPs. **h** Energy difference per formula unit as a function of Q showing the harmonic regime. The blue dots in **(h)** highlight different Q values studied in the previous figures.

to the WTI phase. The energy and bulk band dispersion is symmetric for positive and negative values of Q ; however, the chirality of the WPs and hence the sign of the Berry curvature (BC) changes when Q value changes from positive to negative. This has important implications for the BC-related properties which will be discussed later.

Figure 2 shows the mechanism of formation of the Weyl bands for the lattice distortion corresponding to B_{1u-4} IR mode which is also the lowest optical phonon mode with a frequency of 0.58 THz.

This mode is characterized by the rotational motion of the Te atoms on each $ZrTe_5$ pentamer thereby breaking M_c symmetry which originally is the symmetry of the pentamer (Fig. 1a). Such lattice distortion gives rise to two pairs of WPs for $|Q| \geq 1$ on the k_a - k_b (k_x - k_y) plane. For larger Q values, the WPs move away from the k_y line towards the k_x direction and finally annihilate for $|Q| \geq 5.5$ (Fig. 2a–c, e, f). In addition to the increasing separation between the source and the sinks of the WPs, they also move closer to the Fermi level for higher Q values. Moreover, a nodal

line forms between the valence band and the conduction band pairs. The reason for the formation of the nodal line is due to the broken Kramer's degeneracy of the bands by virtue of the broken inversion symmetry. The two valences (or conduction) bands separate from one another when this happens and their energy surfaces intersect with one another forming a line of degeneracy (nodal line). As it is not protected by any symmetry, for a very large perturbation (i.e., large Q), the nodal line will no longer be present see Supplementary Fig. 6). The charge density plot around the ZrTe₅ pentamer corresponding to the highest occupied (HOMO) and lowest unoccupied (LUMO) states at the Γ -point for $Q = 0$ (i.e., the ground state) and $Q = -4.5$ verifies that there is a charge transfer from Te2 to Te3 atoms mediated by the Zr atoms during this dynamical evolution of the atoms (Fig. 2d). In Fig. 2g, we plot the position of the sources and sinks of the WPs for different Q values on the k_x - k_y plane along with their chiralities which show the evolution of the WPs (i.e., creation, movement, and annihilation). Such dynamical manipulation of the WPs in momentum space could find applications for braiding purposes³² especially if the paths of the different Weyl nodes interchange. This might be possible in the presence of other time-dependent perturbations or if more mirror symmetries are broken in the system dynamically, e.g., by the application of other IR modes. Figure 2h shows the energy cost per formula unit as a function of the lattice distortion corresponding to the B_{1u} -4 mode (expressed in units of Q) which verifies that the system is indeed within the harmonic regime during this dynamical evolution. Similar band plots and analyses for B_{3u} -8 and B_{2u} -20 IR modes are presented in Supplementary Figs. 4 and 5, respectively.

We also studied the possibility of the IR phonon mode induced topological phase transition starting from the WTI phase. The WTI phase was obtained from the application of the A_g -27 phonon mode¹⁸. We find that for the case of the B_{1u} mode, the system does not undergo transition to the Weyl phase irrespective of the proximity of the WTI system to the WTI-STI phase boundary. However, for the case of the B_{3u} mode, such transition is possible if the system is close to the phase boundary. Both observations are consistent with the $k \cdot p$ model [see Eq. (3)]. In the absence of the k -dependent perturbation term, the topological phase transition from the WTI to the Weyl phase is not possible for all the IR phonon modes because band inversion is necessary for such transition. However, the presence of the k -dependent perturbation term allows such transition [see Supplementary Note 2(b) for details].

The critical value of Q required for the formation of the WPs (Q_c) can be decreased if one starts from DSM phase instead of the gapped phase. This is best demonstrated in Fig. 3 with the case of B_{2u} -11 mode, where we see a drastic variation in Q_c : for a gapped STI phase, the system enters the Weyl phase for $Q > 6$ which corresponds to the energy cost of more than 100 meV per formula unit (Fig. 3a, b). However, if the initial phase is a DSM, which can be obtained by the application of resonant A_g Raman modes (the A_g -27 phonon mode was used here¹⁸), then the system enters the Weyl phase for an infinitesimal value of Q (Fig. 3c, d, f). Though not as dramatic, this is also true for the case of B_{1u} -4 mode.

This implies that in pump-probe experiments, a low-power resonant IR light source can drive the system to the Weyl phase if one first prepares the sample to be close to a DSM phase by static perturbations such as strain¹⁵. Another approach is an all-light-controlled ultrafast method, namely, one first applies a laser pumping that excites resonant A_g modes to induce a DSM state, which is metastable with a quasi-static Q_{A_g} value for hundreds of picoseconds^{18–20} and on which the second low-power resonant IR light is applied, as illustrated in Fig. 3g and further analyzed in Eq. (6).

Effective Hamiltonian for IR modes

In order to understand the process of formation of the WPs for all possible IR phonon modes of ZrTe₅, we used the extended $k \cdot p$ model of Chen et al.^{17,33} to devise an effective Hamiltonian describing the essential low energy physics of the STI phase of ZrTe₅ near the Γ -point. The Hamiltonian without inversion symmetry breaking perturbations is:

$$H(k) = (m - Dk^2)\tau^z + v_x k_x \tau^x \sigma^y + v_y k_y \tau^x \sigma^x + v_z k_z \tau^y, \quad (3)$$

where $Dk^2 = D_1 k_x^2 + D_2 k_y^2 + D_3 k_z^2$, σ and τ are the Pauli matrices acting on the spin and valley indices, respectively. The low energy Hamiltonian is derived by enforcing the two mirror symmetries perpendicular to the crystal c -axis and a -axis, M_c and M_a respectively, time-reversal symmetry and inversion symmetry where: $M_c = \tau^z \cdot i\sigma^z$, $M_a = i\sigma^x T = K \cdot i\sigma^y$ and $I = \tau^z$. Because of the presence of the two mirror symmetries and inversion symmetries, the Hamiltonian also has a third symmetry, G_b , a glide symmetry (mirror plus translation parallel to the mirror plane) perpendicular to the b -axis.

The IR phonon modes produce two major effects on Eq. (3): they change m and add inversion symmetry breaking perturbations. Depending on how inversion symmetry is broken, the mirror symmetries are also broken differently for each IR modes. For example, all B_{1u} type IR modes break M_c whereas B_{2u} (B_{3u}) modes break G_b (M_a).

From simple symmetry analysis, it is straightforward to obtain the leading order terms for each of the IR modes. For example, for B_{1u} mode, the k -independent leading order perturbation to Eq. (3) is just $c\tau^x$ where c is a constant. The eigenvalues for this case are given by:

$$E_{\pm}^r = r\sqrt{(m - Dk^2)^2 + \tilde{k}_z^2 + (|\tilde{k}_{xy}|s + c)^2}, \quad (4)$$

where $r, s \in \pm$. The superscript r denotes the valence and conduction states and the subscript s denotes the states within the same branch. Two bands E_{\pm}^+ and E_{\pm}^- cross at zero energy for $k_z = 0$ only if two ellipses of the form:

$$D_1 k_x^2 + D_2 k_y^2 = m, \quad v_x^2 k_x^2 + v_y^2 k_y^2 = c^2 \quad (5)$$

intersect at finite number of k values. Thus formed band touching points are WPs with the linear dispersion in the vicinity of these band touching points, as shown in Supplementary Note 2(a). Using the values of D 's, v 's, and m obtained from fits to the ground state solution (i.e., for $Q = 0$)¹⁸, we find that the two ellipses intersect for $c > 0.01$ thereby giving 4 WPs on the $k_x - k_y$ plane (see Supplementary Fig. 1).

The symmetry considerations dictate that the k -dependent perturbation term for the B_{1u} IR modes can only be of the form $(uk_x \sigma^y + vk_y \sigma^x)\tau^z$ where u and v are constants. Such a term does not create a gap, it only moves the WPs on the $k_x - k_y$ plane. One can perform a similar analyses for other IR modes. The k -independent and dependent perturbation terms for all three types of IR modes are shown in Supplementary Table 3 (See Supplementary Information for discussion about other IR phonon modes, symmetry relationships, and band structure plots.). In the absence of the k -dependent perturbation, the eigenvalues can be found analytically. DFT calculation for the corresponding phonon modes gives the WPs on the same plane found from this simple analysis.

The magnitude as well as variation of the leading-order inversion symmetry breaking perturbation term in the model Hamiltonian (c -value) can be obtained by fitting the DFT eigenvalues in close vicinity of the Γ -point with the analytical results (Table 1) as a function of Q . Figure 3e shows the variation of c and mass m as a function of Q for B_{2u} -11 mode when perturbing the system from the gapped as well as the DSM phase. As expected, c varies almost identically for both cases whereas the m curves have similar behavior but shifted from one-another due

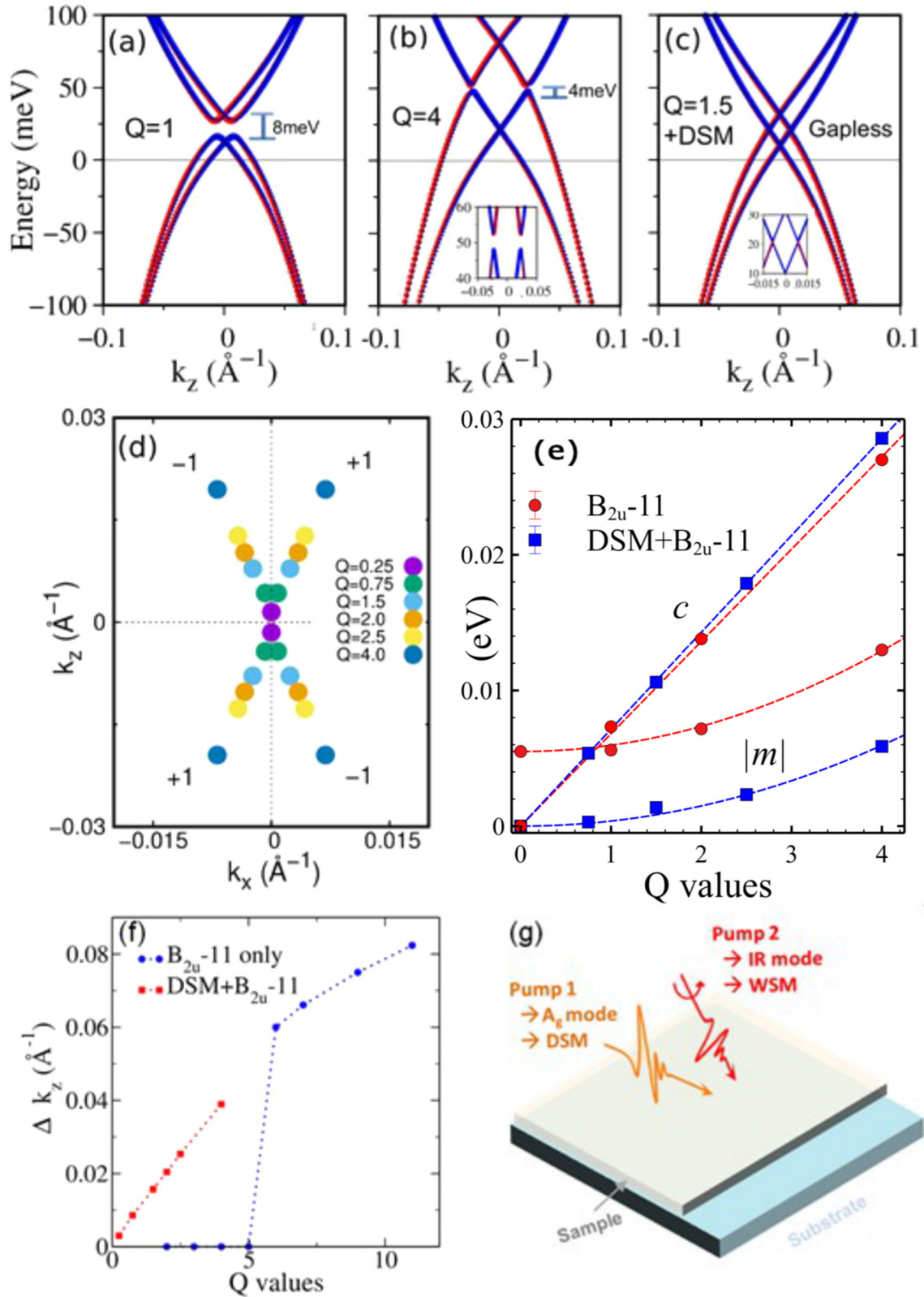


Fig. 3 Weyl bands formation in B_{2u-11} mode. **a–c** Band structure and orbital content of the bands forming the WPs along the k_z direction for: **a** $Q = 1$, **b** $Q = 4$, and **c** $Q = 1.5$ but starting from a DSM phase which was obtained by the application of the A_g-27 phonon mode¹⁸. The insets in **(b)**, **(c)** show zoomed band plots within a narrow energy window of the Weyl bands. **d** Evolution of the WPs as a function of Q when starting from a DSM phase. **e** Variation of the inversion symmetry breaking term c and the mass m as a function of Q obtained by fitting the DFT bands to the eigenvalues from the effective Hamiltonian for B_{2u-11} mode starting from the STI phase (i.e., the ground state) and DSM phase. The dashed lines are fits using Eq. (6). **f** Momentum transfer between the Weyl points as a function of Q for pumping a STI (blue dots) and a DSM (red dots). **g** Schematics of a double-pumping all-light-controlled experiment that utilizes low-power laser sources to drive $ZrTe_5$ into a Weyl state.

Table 1. The inversion symmetry breaking perturbation term for each of the IR modes added to the effective Hamiltonian. $M = (m - Dk^2)^2$, $\tilde{k}_i = v_i k_i$ and $|\tilde{k}_{ij}| = \sqrt{\tilde{k}_i^2 + \tilde{k}_j^2}$.

Model H					
IR mode	Broken symmetry	Constant term	Eigenvalues (E^2)	k-dependent term	WPs location
B_{1u}	M_c	$c\tau^x$	$M^2 + \tilde{k}_z^2 + (\tilde{k}_{xy} \pm c)^2$	$(k_x\sigma^y + k_y\sigma^x)\tau^z$	k_x - k_y plane
B_{2u}	G_b	$c\tau^y\sigma^x$	$M^2 + \tilde{k}_y^2 + (\tilde{k}_{xz} \pm c)^2$	$(k_z\sigma^x + k_x\sigma^z)\tau^z$	k_x - k_z plane
B_{3u}	M_a	$c\tau^y\sigma^y$	$M^2 + \tilde{k}_x^2 + (\tilde{k}_{yz} \pm c)^2$	$(k_y\sigma^z + k_z\sigma^y)\tau^z$	k_y - k_z plane

to the zero mass of the DSM phase. The variation of c and mass m as a function of Q for B_{1u} -4 and B_{3u} -8 are shown in Supplementary Fig. 1.

With the effective Dirac Hamiltonian, one can now understand the multiphonon pumping process proposed above (Fig. 3g). The coupling between the IR and A_g phonon modes can be described by the following Q -dependence of m and c :

$$\begin{aligned} m &= \beta Q_{\text{IR}}^2 + \alpha(Q_{A_g} - Q_0) + \lambda Q_{\text{IR}}^2 Q_{A_g}, \\ c &= \gamma Q_{\text{IR}} + \eta Q_{A_g} Q_{\text{IR}}. \end{aligned} \quad (6)$$

Several remarks about Eq. (6) are presented in passing. First, the linear Q_{A_g} dependence of the α and Q_0 term was demonstrated in ref. 18. Second, c is independent of pure Q_{A_g} terms because the A_g phonon modes do not break inversion symmetry. c is an odd function of Q_{IR} because the chirality of WPs depends on the sign of Q_{IR} . Third, m is an even function of Q_{IR} because $\pm Q_{\text{IR}}$ yield identical band structure at the Γ point [see Eq. (4)]. λ and η denote coupling strengths between the two targeted phonons. While the mode coupling equations could be more complicated, here we consider the simplest possible form. The values of α , Q_0 , β , λ , γ , η in Eq. (6) depend on the phonon modes involved. They can be estimated from fitting the m and c curves, e.g., in Fig. 3e for the coupling between the B_{2u} -11 and A_g -27 modes. The fits (dashed lines) confirm that Eq. (6) contains the leading terms.

Such fitting yields $\alpha = 23 \text{ meV } \text{\AA}^{-1} \text{ amu}^{-\frac{1}{2}}$, $Q_0 = -0.25 \text{ \AA amu}^{\frac{1}{2}}$, $\beta = 0.5 \text{ meV } \text{\AA}^{-2} \text{ amu}^{-1}$, $\lambda = 0.4 \text{ meV } \text{\AA}^{-3} \text{ amu}^{-\frac{3}{2}}$, $\gamma = 6.8 \text{ meV } \text{\AA}^{-1} \text{ amu}^{-\frac{1}{2}}$, and $\eta = -1.6 \text{ meV } \text{\AA}^{-2} \text{ amu}^{-1}$. The contrast of small β vs large γ results from much weaker Q_{IR} dependence of m than c , which means Q_{IR} relatively has little impact on m except when the system is very close to the DSM phase. Moreover, the weak mode coupling manifested by small λ is clearly visible by inspecting the two m curves in Fig. 3e: They look quite similar except for the difference in the y-intercepts (i.e., the α term) due to different Q_{A_g} . These results imply that the harmonic approximation for the phonons holds for the proposed multiphonon pumping.

With the above parameterization, one can study the formation as well as the evolution of the WPs in various combinations of A_g and IR phonon modes. It is now clear that the chirality of the WPs depends only on the sign of c and thus Q_{IR} . Note that for the double-pumping experiment proposed above, ηQ_{A_g} behaves like a constant and is a correction to γ . The sign and magnitude of m do not determine the chirality. Instead, the magnitude of m determines the location of WPs and its sign determines whether WPs can exist: when m is positive (negative), the system is in a STI (WTI) phase which determines whether WPs can exist (or not) upon laser pumping.

Nonlinear Berry curvature effect

It is well known that for systems like ZrTe_5 with both inversion symmetry and time-reversal symmetry, Berry curvature $\Omega(\mathbf{k})$ is identically zero everywhere in the Brillouin zone³⁴. However, when inversion symmetry is broken as is the case here, $\Omega(\mathbf{k})$ is finite and contributes to different transport phenomena. Here, we focus on the second-order effects arising from the Berry curvature such as

photo-galvanic effects and nonlinear anomalous Hall effect (NLAHE). The latter one, unlike the linear AHE, does not require broken time-reversal symmetry³⁵.

The intrinsic contribution (intra-band) to the aforementioned nonlinear effects can be understood in terms of the Berry curvature dipole moment (BCDM). BCDM is dimensionless in three dimension and is zero for a purely isotropic Weyl cone³⁵ (see the Methods section for the definition of BCDM). In ZrTe_5 , because of the presence of the different mirror symmetries, different components of the BCDM are constrained to be zero by symmetry. For example, for B_{1u} mode, the presence of the M_a and G_b symmetry dictates the following transformation rules for the velocities and the BCDM tensor:

$$\begin{aligned} (v_x, v_y, v_z) &\xrightarrow{M_a} (-v_x, v_y, v_z), (v_x, v_y, v_z) \xrightarrow{G_b} (v_x, -v_y, v_z), \\ (\Omega_x, \Omega_y, \Omega_z) &\xrightarrow{M_a} (\Omega_x, -\Omega_y, -\Omega_z), \\ (\Omega_x, \Omega_y, \Omega_z) &\xrightarrow{G_b} (-\Omega_x, \Omega_y, -\Omega_z). \end{aligned} \quad (7)$$

Hence, M_a symmetry constrains all other terms of BCDM to vanish except D_{xy} , D_{yx} , D_{xz} , D_{zx} . Similarly, from G_b symmetry, we find that only D_{xy} , D_{yx} , D_{yz} , D_{zy} survive. Enforcing both M_a and G_b symmetries, only D_{xy} and D_{yx} terms survive for B_{1u} type IR modes. Using similar arguments, we find that for B_{2u} mode, only D_{xz} and D_{zx} terms survive whereas for B_{3u} , D_{yz} and D_{zy} terms survive. This will have nonlinear response along different directions. In the following, we present the results for the BCDM in B_{1u} -4 mode only as its magnitude is larger compared to other modes. This is a direct consequence of the symmetry of the phonon modes and anisotropic band dispersion.

BCDM, being a Fermi surface (FS) property, depends on the shape and size of the FS and the vicinity of the WPs from the FS. Figure 4a-c shows the evolution of the FS for different Q values corresponding to the B_{1u} mode lattice distortion. The FS forms a small hole pocket in the vicinity of the Γ -point; however, its topology changes drastically during this evolution. Moreover, the magnitude of Ω increases during this evolution because the Fermi level shifts closer to the WPs. The magnitude of Ω_y is about 5 times larger compared to Ω_x and Ω_z (see Supplementary Fig. 2). Since both of the factors, v_x and Ω_y that appear in the evaluation of D_{xy} are bigger compared to that of D_{yx} which involves v_y and Ω_x , D_{yx} is negligible compared to D_{xy} .

Figure 4d shows the variation of D_{xy} with the chemical potential (μ) obtained from the ab initio calculation. The value of $\mu = 0$ corresponds to the charge neutral point. The average peak value of D_{xy} (~ 0.05) at $\mu \sim 10 \text{ meV}$ is similar to that of another type-I Weyl semimetal TaP and presumed type-II Weyl semimetal WTe_2 ³⁶. As expected, the peak value of BCDM is concentrated around the WP energy (denoted by the black vertical line in the figure). When μ is right at the WP energy (for $|Q| > 1$) or in the bandgap (for $|Q| < 1$), BCDM vanishes due to the vanishing FS. D_{xy} possesses a striking feature that distinguishes the Weyl from the non-Weyl phase: it changes sign as a function of μ only when the system hosts WPs. The reason for such sign change after crossing the WP energy is simple to understand. It is obvious that the sign of Ω is different for the valence and conduction bands. For example in the 2-band $\sigma \cdot \mathbf{h}(\mathbf{k})$ model with \mathbf{h} being any function of \mathbf{k} , the Berry curvature is given by $\Omega(\mathbf{k})$

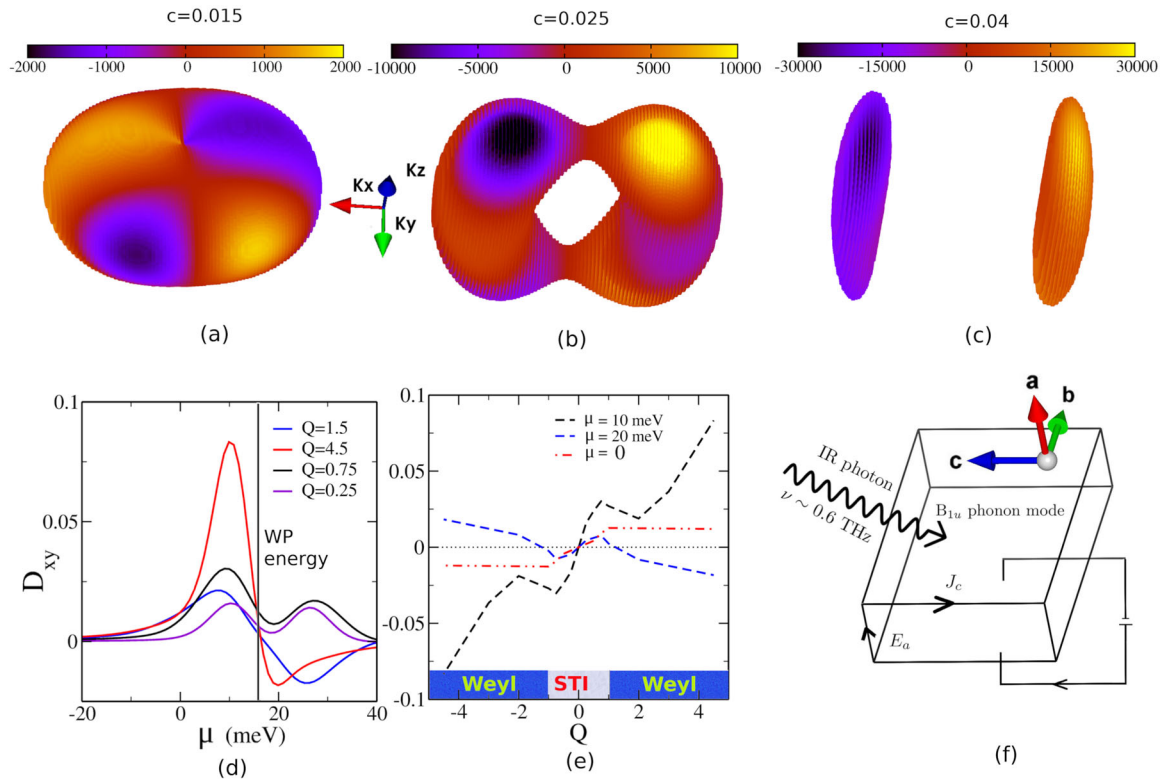


Fig. 4 Berry curvature (BC) and related transport signatures in B_{1u} mode. **a–c** Intensity plot showing the distribution of the Ω_y component of the BC on the FS calculated from the model Hamiltonian for different values of c which roughly corresponds to Q of 1, 2, and 4 respectively. The Fermi level is set from the DFT results. **d, e** D_{xy} component of BCDM as a function of μ and Q respectively calculated using the ab initio Hamiltonian. $\mu = 0$ corresponds to the charge neutral point. The black horizontal line in panel (d) corresponds approximately to WP energy for the case when Weyl points occur whereas for the gapped case, it corresponds to the average of the valence band maximum and conduction band minimum. **f** Schematic diagram of the nonlinear transverse hall response in the presence of an external electric field and inversion symmetry breaking perturbation like B_{1u} phonon mode.

$= \pm \mathbf{k}/k^3$, where \pm are for the valence and conduction bands, respectively. This is also true for band velocity \mathbf{v} when Weyl cone does not have a tilt. However, due to the presence of the k -dependent constant terms, the tilt is finite here and the sign of v_x stays the same. Hence, D_{xy} changes sign upon crossing the WP energy.

In Fig. 4e, we show the variation of BCDM as a function of Q for different values of μ . The asymmetry around $Q=0$ is due to the switching of the chirality between the negative and positive Q values and is present for all values of μ . When μ is positioned at the conduction band, in addition to the sign flip at $Q=0$, D_{xy} changes sign when the system enters the Weyl phase at around Q of 1.5. Hence, depending on the position of the Fermi level, which can be tuned by doping or even temperature^{37,38}. BCDM and the associated currents change sign multiple times as a function of Q .

DISCUSSION

Since only D_{xy} and D_{yx} components of the BCDM are nonzero for B_{1u} mode, from Eq. (8), we find that only non-vanishing components of the conductivity tensor are $\sigma_{xxz} = -\sigma_{zxx}$ from D_{xy} and $\sigma_{zyy} = -\sigma_{yzz}$ from D_{yx} . As D_{yx} is negligible compared to D_{xy} , we focus on the σ component arising from D_{xy} . Since the nonlinear current is given by $j_a = \sigma_{abc} E_b(\omega) E_c^*(\omega)$, $E(\omega)$ being the applied electric field, σ_{zxx} component dictates that application of field along the x -direction (i.e., $b = c = x$) produces a current along the z -direction which amounts to the nonlinear Hall effect in the limit of $\omega \rightarrow 0$. Figure 4f shows schematic diagram of the nonlinear Hall response in the presence of an external transverse electric field and IR photon in resonance with the B_{1u} phonon mode.

Considering the maximum value of D_{xy} of ~ 0.1 and relatively longer relaxation time for the chiral particles $\tau \sim 10$ ps²⁴, we find that a maximum nonlinear Hall current (J_z) of about 2 nA μm^{-2} can be generated in the presence of a typical laboratory electric field (E_x) ~ 100 V m^{-1} and IR photon radiation in resonance with the B_{1u} -4 phonon mode. We note that our predictions regarding BCDM-induced nonlinear anomalous hall currents for different IR phonon modes are also applicable to other static inversion symmetry breaking perturbations, e.g., in the presence of a strong electric field. In that case, the external perturbations breaking inversion symmetry correspond to the linear superposition of the different IR phonon modes which will give rise to BCDM-induced Hall currents in different directions.

The above analysis provides insight into several key observations in recent photocurrent experiments on ZrTe_5 ²⁴, namely, the photocurrent measured by the THz irradiation via circular photogalvanic effect (CPGE) along the crystal a -axis (x -direction) is much larger than that measured along the crystal c -axis (z -direction), while the ratio of the terahertz emission polarization along the z and x -direction E_z/E_x is 9:1. If the dominant IR phonon mode induced by the terahertz pump is indeed B_{1u} -4 as claimed²⁴, then such asymmetry can be understood as follows: The currents along the x and z -directions are given by $j_x = \sigma_{xxz} E_x(\omega) E_z^*(\omega)$ and $j_z = \sigma_{zxx} E_x(\omega) E_x^*(\omega)$, respectively. Hence, it is easy to see that j_x will be significantly higher by 9 times than j_z as $\sigma_{xxz} = -\sigma_{zxx}$.

It is noteworthy that the time average of BCDM appears to vanish, since the BCDM flips sign during the IR phonon vibration due to the chirality flip for $\pm Q$. Thus, the BCDM signal might not be detected in slow bulk measurements. Yet, photocurrents associated with a photoinduced Weyl semimetallic phase in ZrTe_5 have

been observed to last for several picoseconds, much longer lived than the 40fs optical excitations²⁴; therefore, we anticipate observable BCDM signals by ultrafast probes within this picosecond time scale. Equation (6) also suggests that when dynamical Q_{A_g} is involved, the $\eta Q_{A_g} Q_{IR}$ contribution to the WPs could help yield nonzero BCDM signals in an appreciable amount of time when the frequencies of the IR and A_g modes are rather incommensurate with each other. On the other hand, we found that the topological surface states and their spin textures behave differently for positive and negative Q (see Supplementary Fig. 7), giving rise to the possibility of using surface probes to detect BCDM signals over a longer time span. It is intriguing to verify these predictions in future experiments and simulations.

In summary, we find that atomic displacements corresponding to any of the three types of infrared modes of ZrTe₅ can drive the system from a small bandgap topological insulating phase to a Weyl semimetallic phase by breaking the global crystal inversion symmetry in one of the three possible ways. The position of the WPs are constrained by the mirror symmetries, and the WPs remain robust over a large value of the atomic displacements corresponding to the phonon modes. The magnitude of the atomic displacements necessary for driving the system into the Weyl phase can be reduced dramatically if the system is a Dirac semimetallic phase. This can be tested in future experiments by using a relatively lower power resonant IR laser source in conjunction with A_g Raman mode pumps or applying resonant IR laser source to strained ZrTe₅ in close vicinity to the Dirac semimetallic phase. We also find that for the lowest optical phonon mode, the sign of the BCDM, which gives rise to various nonlinear effects, changes upon crossing the Fermi level for only Weyl phase suggesting an experimental way to detect photo-induced Weyl phase in ZrTe₅.

In condensed matter physics, the geometrical chirality of a crystalline electronic system is normally fixed by the chiral lattice structure of a material on formation, when it lacks mirror planes, space-inversion centers, or rotoinversion axes. Dynamic chirality generation by inversion-symmetry breaking paves the way for the development of disorder-tolerant quantum electronics through electromagnetic topology control. While first-principles dynamical simulations are needed to make a more direct comparison with the ultrafast experiments, the present work sheds light on this research direction.

METHODS

First-principles calculations

First-principles density-functional-theory (DFT) calculations were done using Quantum Espresso (QE)³⁹ package. Perdew-Burke-Ernzerhof (PBE) exchange-correlation functional⁴⁰ within the generalized gradient approximation (GGA) were used in all the calculations. Full lattice relaxation and subsequent phonon and electronic band calculations using both QE and VASP packages^{41,42}. For QE, we used fully relativistic norm-conserving pseudopotentials generated using the optimized norm-conserving Vanderbilt pseudopotentials⁴³. The lattice relaxation was performed using Grimme's semi-empirical DFT-D3 vdW interaction as implemented in the QE software as it gave the best agreement with the experimental lattice parameters (with just 3% deviation in volume). The primitive BZ was sampled by using k mesh of $10 \times 10 \times 8$ and energy cutoff of 1000 eV was used after careful convergence tests. For VASP, the optB86b vdW correlation functional was adopted to account for vdW interactions. Density functional perturbation theory (DFPT) method was used to compute the atomic forces as implemented in Phonopy⁴⁴ under the harmonic approximation.

Wannierization method without localization⁴⁵ was employed to extract tight-binding Hamiltonian in the basis of all Zr-*d* and Te-*p* orbitals was subsequently used to find the location of the Weyl nodes by using Wannier Tools package⁴⁶. Berry curvature and related properties were calculated following the Kubo formula as implemented in the Wannier90 package⁴⁷.

The drawings of the crystal structures with phonon modes were produced by using VESTA⁴⁸.

Berry curvature dipole moment

The third rank conductivity tensor associated with the BC effect is defined within the relaxation time approximation as³⁵:

$$\sigma_{abc} = -\frac{e^3 \tau}{2\hbar^2 (1 + i\omega\tau)} \epsilon_{adc} D_{bd}, \quad (8)$$

where, τ is the relaxation time and D_{bdi} , the Berry curvature dipole moment (BCDM) tensor, is in general a function of the chemical potential μ and is given by:

$$D_{ab}(\mu) = \int \frac{d^3 \mathbf{k}}{(2\pi)^3} \sum_n v_a^n(\mathbf{k}) \Omega_b^n(\mathbf{k}) \left(\frac{\partial f_0(E, \mu)}{\partial E} \right)_{E=E_{kn}}. \quad (9)$$

$v_b^n(\mathbf{k})$ is the b^{th} component group velocity of the n^{th} band given by $\frac{\partial E_{nk}}{\partial k_b}$, f_0 is the equilibrium occupation factor and $\Omega_{bc}^n(\mathbf{k}) = \epsilon_{abc} \Omega_d^n(\mathbf{k})$ is given by:

$$\Omega_{ab}^n(\mathbf{k}) = -2 \sum_{m \neq n} \text{Im} \frac{\langle n\mathbf{k} | \hat{v}_a | m\mathbf{k} \rangle \langle m\mathbf{k} | \hat{v}_b | n\mathbf{k} \rangle}{(E_{nk} - E_{mk})^2}, \quad (10)$$

Note that BCDM is a dimensionless quantity in three dimension³⁵. For the calculation of the BCDM, a very dense k-point mesh (up to $300 \times 300 \times 300$) was used to sample a small volume around the Γ -point in order to capture the rapidly varying distribution of the Berry curvature around the regions of band crossings. Energy smearing of 5 meV was used.

The parameters of the effective Hamiltonian [Eq. (3)] were extracted by fitting the analytical eigenvalues with the DFT eigenvalues in close vicinity of the Γ point (up to 0.015 \AA^{-1}). We find that as a function of Q , other parameters of the effective Hamiltonian like D_i and v_i does not vary much as compared to the c and m parameters which is the main effect of the IR phonon modes.

DATA AVAILABILITY

The data that support the findings of this study are available from the corresponding authors upon reasonable request. The data are also accessible at <https://doi.org/10.17172/NOMAD/2022.04.13-1> for the B_{3u-8} phonon mode, <https://doi.org/10.17172/NOMAD/2022.04.13-2> for the B_{2u-11} phonon mode, <https://doi.org/10.17172/NOMAD/2022.04.13-3> for the B_{1u-4} phonon mode.

CODE AVAILABILITY

Quantum Espresso, Wannier90, WannierTools, and VESTA programs used in this work are publicly available.

Received: 6 October 2021; Accepted: 1 May 2022;

Published online: 17 May 2022

REFERENCES

- Hasan, M. Z. & Kane, C. L. Colloquium: Topological insulators. *Rev. Mod. Phys.* **82**, 3045–3067 (2010).
- Armitage, N. P., Mele, E. J. & Vishwanath, A. Weyl and dirac semimetals in three-dimensional solids. *Rev. Mod. Phys.* **90**, 015001 (2018).
- Fu, L. & Kane, C. L. Superconducting proximity effect and majorana fermions at the surface of a topological insulator. *Phys. Rev. Lett.* **100**, 096407 (2008).
- Wiedenmann, J. et al. 4π -periodic josephson supercurrent in hgte-based topological josephson junctions. *Nat. Commun.* **7**, 10303 (2016).
- Nayak, C., Simon, S. H., Stern, A., Freedman, M. & Das Sarma, S. Non-abelian anyons and topological quantum computation. *Rev. Mod. Phys.* **80**, 1083–1159 (2008).
- Kharzeev, D. E. & Li, Q. The chiral qubit: quantum computing with chiral anomaly. Preprint at <https://arxiv.org/abs/1903.07133> (2019).
- Lian, B., Sun, X.-Q., Vaezi, A., Qi, X.-L. & Zhang, S.-C. Topological quantum computation based on chiral majorana fermions. *Proc. Natl Acad. Sci. USA* **115**, 10938–10942 (2018).
- Sie, E. J. et al. An ultrafast symmetry switch in a weyl semimetal. *Nature* **565**, 61–66 (2019).
- Zhang, M. Y. et al. Light-induced subpicosecond lattice symmetry switch in mote₂. *Phys. Rev. X* **9**, 021036 (2019).
- Weber, C. P. Ultrafast investigation and control of dirac and weyl semimetals. *J. Appl. Phys.* **129**, 070901 (2021).

11. Weng, H., Dai, X. & Fang, Z. Transition-metal pentatelluride $ZrTe_5$ and $HfTe_5$: a paradigm for large-gap quantum spin hall insulators. *Phys. Rev. X* **4**, 011002 (2014).
12. Li, Q. et al. Chiral magnetic effect in $ZrTe_5$. *Nat. Phys.* **12**, 550–554 (2016).
13. Manzoni, G. et al. Evidence for a strong topological insulator phase in $ZrTe_5$. *Phys. Rev. Lett.* **117**, 237601 (2016).
14. Xiong, H. et al. Three-dimensional nature of the band structure of $ZrTe_5$ measured by high-momentum-resolution photoemission spectroscopy. *Phys. Rev. B* **95**, 195119 (2017).
15. Mutch, J. et al. Evidence for a strain-tuned topological phase transition in $ZrTe_5$. *Sci. Adv.* **5**, eaav9771 (2019).
16. Xu, B. et al. Temperature-driven topological phase transition and intermediate dirac semimetal phase in $ZrTe_5$. *Phys. Rev. Lett.* **121**, 187401 (2018).
17. Chen, R. Y. et al. Magnetoinfrared spectroscopy of landau levels and zeeman splitting of three-dimensional massless dirac fermions in $ZrTe_5$. *Phys. Rev. Lett.* **115**, 176404 (2015).
18. Aryal, N., Jin, X., Li, Q., Tselik, A. M. & Yin, W. Topological phase transition and phonon-space dirac topology surfaces in $ZrTe_5$. *Phys. Rev. Lett.* **126**, 016401 (2021).
19. Konstantinova, T. et al. Photoinduced dirac semimetal in $ZrTe_5$. *npj Quantum Mater.* **5**, 80 (2020).
20. Vaswani, C. et al. Light-driven raman coherence as a nonthermal route to ultrafast topology switching in a dirac semimetal. *Phys. Rev. X* **10**, 021013 (2020).
21. Murakami, S. Phase transition between the quantum spin hall and insulator phases in 3d: emergence of a topological gapless phase. *New J. Phys.* **9**, 356–356 (2007).
22. Halász, G. B. & Balents, L. Time-reversal invariant realization of the weyl semimetal phase. *Phys. Rev. B* **85**, 035103 (2012).
23. Wang, L.-L. Expansive open fermi arcs and connectivity changes induced by infrared phonons in $ZrTe_5$. *Phys. Rev. B* **103**, 075105 (2021).
24. Luo, L. et al. A light-induced phononic symmetry switch and giant dissipationless topological photocurrent in $ZrTe_5$. *Nat. Mater.* **20**, 329–334 (2021).
25. Asnin, V. et al. "circular" photogalvanic effect in optically active crystals. *Solid State Commun.* **30**, 565–570 (1979).
26. Belinicher, V. I. & Sturman, B. I. The photogalvanic effect in media lacking a center of symmetry. *Sov. Phys. Uspekhi* **23**, 199–223 (1980).
27. Hübener, H., Sentef, M. A., De Giovannini, U., Kemper, A. F. & Rubio, A. Creating stable floquet-weyl semimetals by laser-driving of 3d dirac materials. *Nat. Commun.* **8**, 13940 (2017).
28. Wang, Z. et al. Dirac semimetal and topological phase transitions in A_3Bi ($a = Na, K, Rb$). *Phys. Rev. B* **85**, 195320 (2012).
29. Liu, Z. K. et al. Discovery of a three-dimensional topological dirac semimetal, Na_3Bi . *Science* **343**, 864–867 (2014).
30. Ideue, T. et al. Bulk rectification effect in a polar semiconductor. *Nat. Phys.* **13**, 578–583 (2017).
31. Zwick, A., Landa, G., Carles, R., Renucci, M. & Kjekshus, A. Lattice modes in the linear chain compound $ZrTe_5$. *Solid State Commun.* **44**, 89–94 (1982).
32. Trevisan, T. V., Arribi, P. V., Heinonen, O., Slager, R.-J. & Orth, P. P. Bicircular light floquet engineering of magnetic symmetry and topology and its application to the dirac semimetal Cd_3As_2 . *Phys. Rev. Lett.* **128**, 066602 (2022).
33. Choi, Y., Villanova, J. W. & Park, K. Zeeman-splitting-induced topological nodal structure and anomalous hall conductivity in $ZrTe_5$. *Phys. Rev. B* **101**, 035105 (2020).
34. Xiao, D., Chang, M.-C. & Niu, Q. Berry phase effects on electronic properties. *Rev. Mod. Phys.* **82**, 1959–2007 (2010).
35. Sodemann, I. & Fu, L. Quantum nonlinear hall effect induced by berry curvature dipole in time-reversal invariant materials. *Phys. Rev. Lett.* **115**, 216806 (2015).
36. Zhang, Y., Sun, Y. & Yan, B. Berry curvature dipole in weyl semimetal materials: an ab initio study. *Phys. Rev. B* **97**, 041101 (2018).
37. Zhang, Y. et al. Electronic evidence of temperature-induced lifshitz transition and topological nature in $ZrTe_5$. *Nat. Commun.* **8**, 15512– (2017).
38. Chi, H. et al. Lifshitz transition mediated electronic transport anomaly in bulk $ZrTe_5$. *New J. Phys.* **19**, 015005 (2017).
39. Giannozzi, P. et al. Quantum espresso: a modular and open-source software project for quantum simulations of materials. *J. Condens. Matter Phys.* **21**, 395502 (19pp) (2009).
40. Perdew, J. P., Burke, K. & Ernzerhof, M. Generalized gradient approximation made simple. *Phys. Rev. Lett.* **77**, 3865–3868 (1996).
41. Kresse, G. & Hafner, J. Ab initio molecular dynamics for liquid metals. *Phys. Rev. B* **47**, 558–561 (1993).
42. Blöchl, P. E. Projector augmented-wave method. *Phys. Rev. B* **50**, 17953–17979 (1994).
43. Hamann, D. R. Optimized norm-conserving vanderbilt pseudopotentials. *Phys. Rev. B* **88**, 085117 (2013).
44. Togo, A. & Tanaka, I. First principles phonon calculations in materials science. *Scr. Mater.* **108**, 1–5 (2015).
45. Mostofi, A. A. et al. An updated version of wannier90: a tool for obtaining maximally-localised wannier functions. *Comput. Phys. Commun.* **185**, 2309–2310 (2014).
46. Wu, Q., Zhang, S., Song, H.-F., Troyer, M. & Soluyanov, A. A. Wanniertools: an open-source software package for novel topological materials. *Comput. Phys. Commun.* **224**, 405–416 (2018).
47. Tsirkin, S. S., Puente, P. A. & Souza, I. Gyrotropic effects in trigonal tellurium studied from first principles. *Phys. Rev. B* **97**, 035158 (2018).
48. Momma, K. & Izumi, F. VESTA 3 for three-dimensional visualization of crystal, volumetric and morphology data. *J. Appl. Crystallogr.* **44**, 1272–1276 (2011).

ACKNOWLEDGEMENTS

This work was supported by the U.S. Department of Energy (DOE) the Office of Basic Energy Sciences, Materials Sciences, and Engineering Division under Contract No. DE-SC0012704. X.J. acknowledges the visiting scholarship of Brookhaven National Laboratory and the financial support of the China Scholarship Council and the National Natural Science Foundation of China (No. 11774119). M.L. acknowledges support from the NSF Faculty Early Career Development Program under Grant No. DMR-2045425.

AUTHOR CONTRIBUTIONS

W.Y., N.A., and Q.L. designed the project. N.A. performed the first-principles electronic band structure calculations and effective Hamiltonian analysis. X.J. performed the full lattice relaxation and phonon calculations. A.T. and M.L. provided theoretical and experimental insights, respectively. All authors contributed to the analysis and discussion of the results. N.A. and W.Y. wrote the manuscript with input from all coauthors.

COMPETING INTERESTS

The authors declare no competing interests.

ADDITIONAL INFORMATION

Supplementary information The online version contains supplementary material available at <https://doi.org/10.1038/s41524-022-00800-z>.

Correspondence and requests for materials should be addressed to Niraj Aryal or Weiguo Yin.

Reprints and permission information is available at <http://www.nature.com/reprints>

Publisher's note Springer Nature remains neutral with regard to jurisdictional claims in published maps and institutional affiliations.



Open Access This article is licensed under a Creative Commons Attribution 4.0 International License, which permits use, sharing, adaptation, distribution and reproduction in any medium or format, as long as you give appropriate credit to the original author(s) and the source, provide a link to the Creative Commons license, and indicate if changes were made. The images or other third party material in this article are included in the article's Creative Commons license, unless indicated otherwise in a credit line to the material. If material is not included in the article's Creative Commons license and your intended use is not permitted by statutory regulation or exceeds the permitted use, you will need to obtain permission directly from the copyright holder. To view a copy of this license, visit <http://creativecommons.org/licenses/by/4.0/>.

© The Author(s) 2022